Mechanics of two filaments in tight orthogonal contact

Paul Grandgeorge[a,1], Changyeob Baek[a,b,1], Harmeet Singh[c], Paul Johanns[a], Tomohiko G. Sano[a], Alastair Flynn[c], John H. Maddocks[c,2], and Pedro M. Reis[a,2]

[a]Flexible Structures Laboratory, Institute of Mechanical Engineering, École Polytechnique Fédérale de Lausanne, Lausanne 1015, Switzerland; [b]Department of Mechanical Engineering, Massachusetts Institute of Technology, Cambridge, MA 02139; and [c]Laboratory for Computation and Visualization in Mathematics and Mechanics, Institute of Mathematics, École Polytechnique Fédérale de Lausanne, Lausanne 1015, Switzerland

Edited by David A. Weitz, Harvard University, Cambridge, MA, and approved March 7, 2021 (received for review October 17, 2020)

Networks of flexible filaments often involve regions of tight contact. Predictively understanding the equilibrium configurations of these systems is challenging due to intricate couplings between topology, geometry, large nonlinear deformations, and friction. Here, we perform an in-depth study of a simple, yet canonical, problem that captures the essence of contact between filaments. In the orthogonal clasp, two filaments are brought into contact, with each centerline lying in one of a pair of orthogonal planes. Our data from X-ray tomography (μCT) and mechanical testing experiments are in excellent agreement with finite element method (FEM) simulations. Despite the apparent simplicity of the physical system, the data exhibit strikingly unintuitive behavior, even when the contact is frictionless. Specifically, we observe a curvilinear diamond-shaped ridge in the contact-pressure field between the two filaments, sometimes with an inner gap. When a relative displacement is imposed between the filaments, friction is activated, and a highly asymmetric pressure field develops. These findings contrast to the classic capstan analysis of a single filament wrapped around a rigid body. Both the μCT and FEM data indicate that the cross-sections of the filaments can deform significantly. Nonetheless, an idealized geometrical theory assuming undeformable tube cross-sections and neglecting elasticity rationalizes our observations qualitatively and highlights the central role of the small, but nonzero, tube radius of the filaments. We believe that our orthogonal clasp analysis provides a building block for future modeling efforts in frictional contact mechanics of more complex filamentary structures.

elastic structures | Kirchhoff rods | knots | capstan equation | contact mechanics

Flexible filamentary structures have been handcrafted and employed by humans since prehistoric times for fastening, lifting, hunting, weaving, sailing, and climbing (1). The associated engineering of ropes and fabrics has evolved substantially (2), reflecting the need to predict and enhance their mechanical performance (e.g., flexibility, strength, and durability). Toward rationalizing the behavior of touching filaments, pioneering contributions on the mechanics of one-dimensional (1D) structures [e.g., the Euler elastica (3, 4) and the Kirchhoff theory of rods (5, 6)] have been gradually augmented to describe more complex assemblies of filaments, including frictional elastica (7); plant tendrils (8); knitted (9) and woven (10, 11) fabrics; gridshells (12, 13); networks (14); filament and wire bundles (15–20); and knots (both loose and tight) (21–26). However, notwithstanding centuries of advances in the mechanics of filamentary networks across length scales, the descriptive understanding of tight filament–filament interactions remains intuitive and empirical at best. In these systems, the intricate coupling between the highly nonlinear fiber deformations, their contact geometry, and mechanics limits the applicability of conventional 1D centerline-based models, such as the Kirchhoff or other rod-based frameworks, whenever the small, but positive, size of the tube cross-section is not explicitly considered.

Here, we study a deceptively simple, yet, we believe, canonical, system comprising the mechanical contact between two elastic rods, whose respective centerlines lie in one of two orthogonal planes (Fig. 1*A*), a problem that we refer to as the *elastic orthogonal clasp*. Using precision X-ray tomography (μCT; Fig. 1*B*) and the finite element method (FEM; Fig. 1*C*), we first study the contact equilibria of a physical elastic clasp under quasistatic conditions, where friction can reasonably be neglected. Throughout, we find excellent quantitative agreement between experiment and FEM computations. For example, both predict that the two tubular rod surfaces touch in a saddle-shaped *patch*. The FEM simulations additionally give access to the pressure distribution in the contact region between the rods. For a wide range of loading regimes, the pressure distribution is strongly heterogeneous and highly localized along ridgelines that link four isolated peaks, forming a twofold symmetric, curvilinear diamond pattern. This surprising localization can be explained qualitatively by using a version of a 1D, primarily geometrical theory, called the *ideal orthogonal clasp*. This 1D theory exhibits contact *lines* (cf. Fig. 1*D*), which form a remarkably accurate skeleton of the ridgelines

Significance

Knots, knits, and weaves have been technologically essential across civilizations, and their significance remains undiminished today. In these systems, it is challenging to understand the equilibria of the deformable filaments with their tight contacts due to the intricate geometry of touching tubular volumes of small, but nonvanishing, radius. This article considers a specific canonical context for filaments in contact: the orthogonal clasp. We quantify the significant mismatches between the physical reality of orthogonal clasps and the simplifying assumptions underpinning conventional descriptive models, such as the classic capstan equation. Nevertheless, we show that a simple, geometric model qualitatively captures the striking localization patterns in the observed contact-pressure fields.

Author contributions: J.H.M. and P.M.R. designed research; P.G., C.B., H.S., P.J., T.G.S., and A.F. performed research; P.G., C.B., H.S., J.H.M., and P.M.R. analyzed data; P.G., C.B., H.S., P.J., T.G.S., J.H.M., and P.M.R. wrote the paper; P.G. performed experiments; C.B. performed simulations; H.S. and J.H.M. developed the theoretical model; P.J. developed the fabrication protocol; and P.J. and T.G.S. developed the imaging protocol and image-processing algorithm.

The authors declare no competing interest.

This article is a PNAS Direct Submission.

[1]P.G. and C.B. contributed equally to this work.

[2]To whom correspondence may be addressed. Email: pedro.reis@epfl.ch or john.maddocks@epfl.ch.

This article contains supporting information online at https://www.pnas.org/lookup/suppl/doi:10.1073/pnas.2021684118/-/DCSupplemental.

Published April 5, 2021.

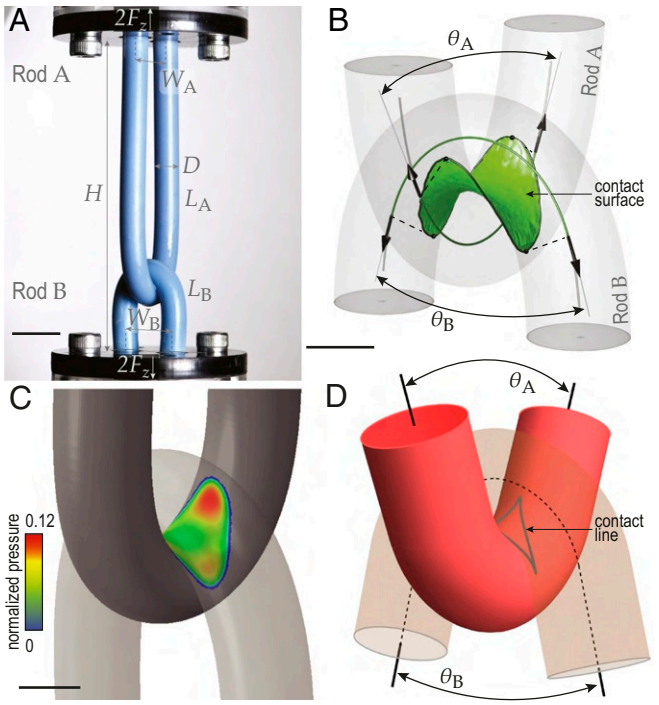

Fig. 1. The orthogonal clasp: two rods in physical contact. (*A*) Photograph of an elastic orthogonal clasp: Two homogeneous rods (A and B) lying in orthogonal planes are brought into contact. Both rods have a rest diameter D, respective rest lengths L_A and L_B, and their extremities are fixed at distances W_A and W_B apart. The loading is performed by varying the wall-to-wall distance H. (Scale bar: 20 mm.) (*B*) Tomographic rendering of the elastic clasp in the vicinity of the contact surface obtained from μCT. The physical centerlines of the rods are represented as thin dark gray tubes. The local opening angles of the two rods, θ_A and θ_B, are defined as the angle between the two tangents (black arrows) to the respective centerlines at the extremities of the (green) portions of the centerline attributed to the contact (or green) surface. (Scale bar: 5 mm.) (*C*) Corresponding FEM computation of the elastic orthogonal clasp for the same parameters as in *B*. The color map represents the contact-pressure distribution (normalized by EA/D^2) between the two rods. (Scale bar: 5 mm.) (*D*) Equilibrium configuration of an ideal orthogonal clasp with two perfectly flexible tubes in contact. The tubes have circular cross-sections orthogonal to the centerline. The idealized contact set is a closed, curvilinear diamond-shaped line, meaning that there is a gap region between the tips of the two tubular surfaces. All configurations in *A*–*C* were obtained for the same physical parameters: $D = 8.5$ mm, $L_A = 170$ mm, $W_A = 17$ mm, $L_B = 63.7$ mm, $W_B = 17$, and $H = 103.2$ mm. The ideal clasp in *D* was computed for the local opening angles, θ_A and θ_B, measured on the elastic clasp of *A*–*C* ($\theta_A = 58°$ and $\theta_B = 33°$).

of the FEM pressure field computed for the elastic orthogonal clasp. The accuracy of this approximation is all the more remarkable, given that the ideal clasp model assumes undeformable tube cross-sections, while both experiment and FEM simulation reveal significant deformations of cross-sections in the elastic clasp. Finally, we investigate the effect of friction by carrying out capstan-inspired experiments, where one of the elastic rods in the clasp is made to slide against the other. We find that the local contact mechanics strongly influences the tension drop along the sliding rod and that the contact-pressure field now only exhibits three peaks. We provide a qualitative explanation of these observations by considering the analogous system of a V-belt capstan problem built from the ideal orthogonal clasp case. Overall, our findings demonstrate the central role played by the small, but nonvanishing, tube radius in the underlying complex geometry of two contacting filaments in dictating their mechanical response.

Contact Surface of the Elastic Orthogonal Clasp

Fig. 1*A* presents the experimental setup that we designed to study elastic orthogonal clasps systematically. We clamped two homogeneous elastic rods, rod A and rod B, to two rigid walls, the distance between which (H) is varied to bring the rods into contact. The two rods have equal rest diameters D, respective rest lengths L_A and L_B, and their extremities are clamped at distances W_A and W_B apart. As the imposed wall-to-wall distance H is varied, the overall geometry of the elastic clasp changes. Each wall applies a total vertical force of $2F_z$ to the elastic clasp (F_z per extremity). We define the normalized vertical force $f_z = F_z/EA$, where E is Young's modulus of the material and $A = \pi D^2/4$ is the unloaded rod cross-section area. The experiments enabled us to investigate the contact geometry between the touching rods by analyzing the μCT volumetric images of tomographically scanned elastic clasps. To enable such a three-dimensional (3D) image analysis, we customized a rod-fabrication protocol (detailed in *SI Appendix*, section 1.A) to produce (coaxial) composite rods. These rod designs, together with μCT, enabled the precise determination of the material centerlines of each rod, along with the contact-surface geometry between the rods.

In Fig. 1*B*, we show a representative example of a rendered 3D μCT image of an elastic clasp, along with rod centerlines and contact surface (*Materials and Methods*, *SI Appendix*, sections 1.B and 1.C, and Movies S1 and S2). The saddle-shaped contact surface, physically hidden in between the two rods, is the primary object of our study. In parallel to our experimental investigation, we conducted full 3D simulations using the FEM to extract quantities that were not readily available from the experiment, with particular focus on the contact pressure between the rods (color bar in Fig. 1*C*). In *SI Appendix*, section 3, we detail our validation procedure of the FEM numerics using the force-displacement curves, $F_z(H)$, for the clasp configuration presented Fig. 1*A* (see also Movie S3). Beyond the precise localization of the saddle-shaped contact surface, our computational FEM procedure reveals a highly heterogeneous pressure field between the two rods, which we will analyze in detail. One of the central goals of our study is to obtain a qualitative rationalization of the features observed in this pressure field using the highly simplified, purely geometric theory of idealized orthogonal clasps.

The Geometrical Theory of Idealized Orthogonal Clasps

The geometrical problem of predicting contact sets between tightly interwound filaments subject to a nonpenetration constraint has been addressed previously in the context of ideal knot shapes—for example, refs. 27 and 28—where it was observed that it is common for double-contact lines to arise. Ideal shapes involve filaments that, by assumption, have undeformable, circular, orthogonal cross-sections of finite radius. Typically, ideal knot problems are formulated as a purely geometrical problem with no mechanics, which corresponds to their centerlines being considered as inextensible, yet perfectly flexible, so that they can support no bending moment. Starostin (29) first considered the particular case of the ideal shape of an orthogonal clasp, but only for the fourfold symmetric case, where the two components are congruent. In our notation, Starostin assumed that the two local opening angles (defined in Fig. 1*D*) were equal $\theta_A = \theta_B$. In *Materials and Methods* and *SI Appendix*, section 4.D, we present a self-contained variant of Starostin's analysis that allows for an explicit computation of the contact set (e.g., Fig. 1*D*), including the cases $\theta_A \neq \theta_B$, via the numerical solution of a set of ordinary differential equations (see additional computation results in Movie S4). For each $0 \leq \theta_A, \theta_B < \pi$, the contact set is a closed, curvilinear, diamond-shaped line, which stands in contrast to the surface-patch contact set observed in both the experimental μCT and numerical FEM data for the elastic orthogonal clasp (where

cross-sections are deformable; Fig. 1 *B* and *C*). A significant part of our study seeks to explain the connection between the contact patches observed for elastic orthogonal clasps and the contact lines predicted by the ideal orthogonal clasp model.

Double-contact lines arise in ideal knot shapes when, at arc-length s_1 along the tube centerline, the corresponding circular arc in the tube surface has two contact points with other surface arcs, each of which correspond to another two distinct centerline arc-lengths, s_2 and s_3, say. The straight line segment connecting two points on the knot centerline with such pairs of arc lengths (s_1, s_2), or (s_1, s_3), is referred to as a *contact chord* (cf. *SI Appendix*, Fig. S15). This double-contact feature is found in the present case of the ideal orthogonal clasp, where the phenomenon is perhaps less surprising due to the presence of two planes of reflectional symmetry. Moreover, due to the reflection symmetry, the set of all contact chords decomposes into a one-parameter family of closed equilateral tetrahedra. It is the one-parameter family of midpoints of these four tetrahedral edges that traces out the curvilinear, diamond-shaped contact line. The corners of the diamond arise when the family of open tetrahedra collapses to two double-covered straight line segments. In turn, this coalescent limit arises at first and last contact points along the curve centerlines (or touch-down and lift-off points; cf. *SI Appendix*, section 4.D for more details). The diamond-shaped contact line surrounds the two tips of the clasp equilibria, and, consequently, there is always an enclosed gap, or physical space, separating the two tubes close to their tips, except in degenerate cases, where one or both tubes have vanishing curvature at their tip.

Heuristically, the connection between the contact lines of the ideal orthogonal clasp and the contact patches of the elastic orthogonal clasp can be explained, in both experiment and FEM, by cross-section deformation. Consequently, the idealized contact lines are, in reality, "fattened" to become surface patches. In general, the deformation of the cross-sections can be sufficiently large that the small gap between the tips of the ideal orthogonal clasp can close in the corresponding elastic orthogonal clasp. Nevertheless, in most cases, we do observe an overall resemblance between the shape of the ideal contact line and the boundary of the elastic clasp surface patch, as in Fig. 1 *B–D* (see Movie S1 for a full 3D view of the contact region). In our consideration of the four cases illustrated in Fig. 2, we observed one elastic clasp configuration in which the tip gap did persist (Fig. 3*B2*). Furthermore, we will show below that, in many cases, the pressure distribution in our FEM simulations of the elastic orthogonal clasp are highly concentrated on the diamond-shaped contact lines in the corresponding ideal orthogonal clasp and that these high pressures arise toward the boundary of the contact patch, with comparatively low contact pressures close to the central tip regions.

Local Opening Angles of the Elastic Clasp

Next, we make a more detailed comparison between corresponding equilibria of the ideal and elastic orthogonal clasp configurations. To identify corresponding cases, we use the local opening angles θ_A and θ_B, defined as the angle described by the tangents to the centerlines of either the tube (for the ideal case) or rod (for the elastic case) at the touch-down and lift-off contact points (Fig. 1 *B* and *D*). Since these angles appear in both cases, we can take them as the common denominator to identify corresponding equilibria. In the ideal orthogonal clasp, these two local opening angles are the only model input parameters; the tube diameter and the magnitude of the tensions applied at the tube ends are scale factors. Moreover, because segments of ideal equilibria that are not in contact have straight centerlines, the local opening angles equal the constant, global opening angles between tail segments far from contact. However, this is no longer true in the elastic orthogonal clasp, where the presence of bending stiffness implies that the global angle between two tail regions is not constant, and, in particular, the global and local opening angles can differ significantly. In the elastic orthogonal clasp, the inputs are the applied vertical load (or the vertical imposed displacement) and the horizontal displacement boundary conditions enforced at the ends of both rods. For the elastic orthogonal clasp, the two local opening angles are observables, which can be measured experimentally from the μCT data or computed as part of the FEM simulation. As we will discuss further below, it is also the local opening angles that are of key importance when describing the frictional mechanics of touching filaments, because they reflect the extent of the contact region.

In Fig. 2 *A–D*, we present four different configurations of displacement boundary conditions that we employed to explore a range of local opening angles (the details of each configuration are provided in the legend of Fig. 2). The corresponding curves for θ_A and θ_B, as functions of the normalized vertical load f_z, for these four configurations are provided in Fig. 2 *E* and *F* for experiment (datapoints) and simulation (solid lines; the small squiggles in the FEM data are due to the discrete nature of the underlying numerical mesh). We note that the local opening angles computed using FEM are in excellent agreement with the experimental measurement. As expected, in all four cases, the local opening angles of rods A and B decrease monotonically as f_z increases; the clasp configurations become tighter.

Interestingly, the $\theta_A(f_z)$ response is largely independent of the geometric conditions imposed on rod B and vice versa. Indeed, in configurations 1, 2, and 3, rod A has the same imposed boundary conditions; even though it is in contact with rods B of different lengths subject to different boundary conditions, it exhibits a nearly identical $\theta_A(f_z)$ curve across these three configurations. Motivated by this observation, we sought to predict the local opening-angle response based on a simplified theory of a single Kirchhoff elastic rod wrapped around a rigid, right circular cylinder of diameter D. Full details of this simplified theory are provided in *Materials and Methods* and in *SI Appendix*, sections 4.A and 4.C. The Kirchhoff-based predictions, dashed lines in Fig. 2 *E* and *F*, show a significant mismatch with the measured local opening angles (experiments and FEM). We conclude that this simple theoretical approximation is inadequate, which will be consequential when we model the frictional sliding clasp below.

The standard Kirchhoff rod model is based on the assumptions (or approximations) that cross-sections are undeformable and unshearable (30). In the *SI Appendix*, section 2, we quantify the cross-section deformation, the centerline curvature, and the shear strain along the centerline of rod A, taking configuration 3 as a representative case. We observe that, even at the relatively low load $f_z = 0.05$, all of these quantities reach substantial values in the neighborhood of contact. First, the cross-section can deform significantly, flattening from its original circular shape by up to 10%. Secondly, the radius of the centerline curvature approaches the rod diameter. Finally, the shear strain reaches values up to 10%. Therefore, in the elastic clasp, the Kirchhoff rod approximations are not accurate. Nevertheless, as we demonstrate next, the alternative 1D geometric theory of the idealized orthogonal clasp, with its detailed treatment of the contact geometry, does provide a framework within which to successfully construct a qualitative explanation of the skeleton of the contact-pressure distribution that is observed for the 3D elastic orthogonal clasp.

Distributions of the Contact Pressure

We proceed by analyzing the pressure distribution in the contact region of elastic orthogonal clasps. By way of example, we focus on the three representative cases of imposed boundary

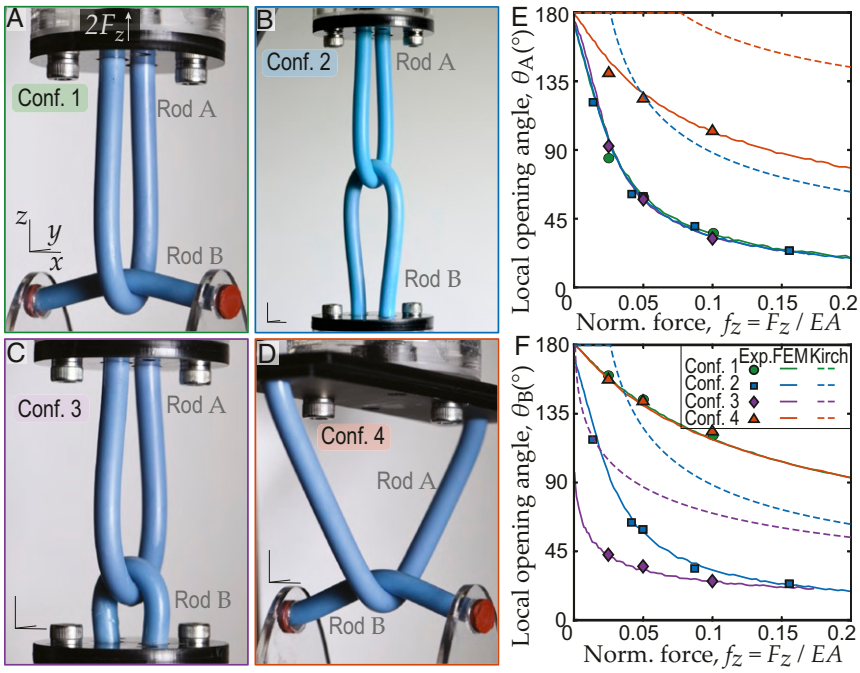

Fig. 2. Local opening angles of the elastic orthogonal clasp, as a function of applied load, for four specific configurations of displacement boundary conditions. (*A*) The elastic rods of configuration (Conf.) 1 have the following normalized geometric attributes: rod A, $l_A = L_A/D = 20$, $w_A = W_A/D = 2$; rod B, $l_B = L_B/D = 7.5$, $w_B = W_B/D = 7.5$ (rod B is straight when no load is applied). (*B*) Configuration 2: rod A, $l_A = 20$, $w_A = 2$; rod B, $l_B = 20$, $w_B = 2$. (*C*) Configuration 3: rod A, $l_A = 20$, $w_A = 2$; rod B, $l_B = 7.5$, $w_B = 2$. (*D*) Configuration 4: rod A, $l_A = 20$, $w_A = 14$; rod B, $l_B = w_B = 7.5$ (rod B is straight when load is applied). (Length of the lines representing the *x*, *y*, *z* directions in *A*–*D*: 10 mm.) (*E* and *F*) Local opening angles θ_A (*E*) and θ_B (*F*) plotted versus the normalized (Norm.) applied vertical force f_z. The experimental local opening angles (data points, measured through μCT tomography) and the FEM simulations (solid lines) are in excellent agreement. In all cases, the local opening angles systematically decrease as the load f_z increases. A simplified capstan computation of local opening angles derived from a single elastic rod wrapped around a rigid straight cylinder in the absence of friction (dashed lines) delivers rather poor predictions, which reflects the need for a more detailed model of the contact geometry.

conditions shown in Fig. 3, each at three different values of the normalized applied loads ($f_z = \{0.005, 0.05, 0.15\}$). The three configurations considered are: a pair of long rods ($l_A = l_B = 20$ and $w_A = w_B = 2$; Fig. 3*A1*), a pair of short rods ($l_A = l_B = 7.5$ and $w_A = w_B = 2$; Fig. 3*B1*), and a combination of the long and short rods ($l_A = 20$, $l_B = 7.5$ and $w_A = w_B = 2$; Fig. 3*C1*), where the physical configurations shown correspond to the low applied load $f_z \simeq 0.005$. For each of the nine cases, the contact-pressure maps are computed by using FEM simulation and then compared with both the extent of the corresponding contact surface patch measured from the μCT experiments and the contact line predicted by the ideal orthogonal clasp analysis.

The contact pressure is computed from the FEM data as the normal force per unit area on the contact surface patch embedded in 3D. However, for visualization purposes, this scalar field is plotted as a color map in the two-dimensional parameter space ($s_A = S_A/D$, $s_B = S_B/D$); the normalized arc lengths along the two rod centerlines provide a coordinate system for the contact surface patch (Fig. 3 *A2*–*A4*, *B2*–*B4*, and *C2*–*C4*). The point $s_A = s_B = 0$ corresponds to the apices of the rods. With this parameterization, it is possible to overlay the boundaries of the contact region extracted from the μCT experiments of the elastic clasp configuration on the analogous FEM computations with the same local opening angles (dashed lines); excellent agreement is found between the two. In these plots, we also juxtapose the contact line predicted by the ideal orthogonal clasp theory (solid black lines in Fig. 3 *A2*–*A4*, *B2*–*B4*, and *C2*–*C4*). All three equilibria for the first two sets of boundary conditions exhibit fourfold symmetric contact-pressure maps ($\theta_A = \theta_B$). By contrast, there is only twofold symmetry for the third configuration ($\theta_A \neq \theta_B$). The contact pressures are highly heterogeneous. For instance, Fig. 3*C3* shows four pressure peaks near the entrance and exit regions of contact along the two rods, connected by ridges of high-pressure values (solid blue lines). To construct points along the ridge in the pressure map, we located 1D local maxima in pressure when evaluated along 720 radial straight lines emanating from the (0, 0) origin point.

Remarkably, for all three cases of moderate loading $f_z \simeq 0.05$ presented in Fig. 3, the pressure ridges closely follow the curvilinear, diamond-shaped contact line predicted by the ideal clasp geometric theory (solid black lines) for the same pair of local opening angles; the four peaks in pressure are close to the four corners of the diamond. In these three cases, the purely geometric ideal clasp model provides an accurate skeleton of the pressure map in the physical system. Due to the deformability of the rod cross-sections, the singular, linear pressure field (force per unit length) predicted from geometry is smoothed out to yield the ridges in the surface pressure (force per unit area) for the elastic orthogonal clasp. In the case of higher loading ($f_z \simeq 0.15$; Fig. 3 *A4*, *B4*, and *C4*), where there is significant deformation in the rod cross-sections, the surface pressure becomes more uniform over the interior of the region of contact, and the ridges are no longer observed.

The case of small loading ($f_z \simeq 0.005$; Fig. 3 *A2*, *B2*, and *C2*) reveals a variety of contact-pressure distributions depending on the global geometry of the equilibrium. Fig. 3*A2* shows a highly localized pressure map, characterized by a single peak close to the apices $s_A = s_B = 0$. However, in Fig. 3*B2*, both pressure ridges and a central region of vanishing pressure are observed, corresponding closely to the predictions of the ideal orthogonal clasp

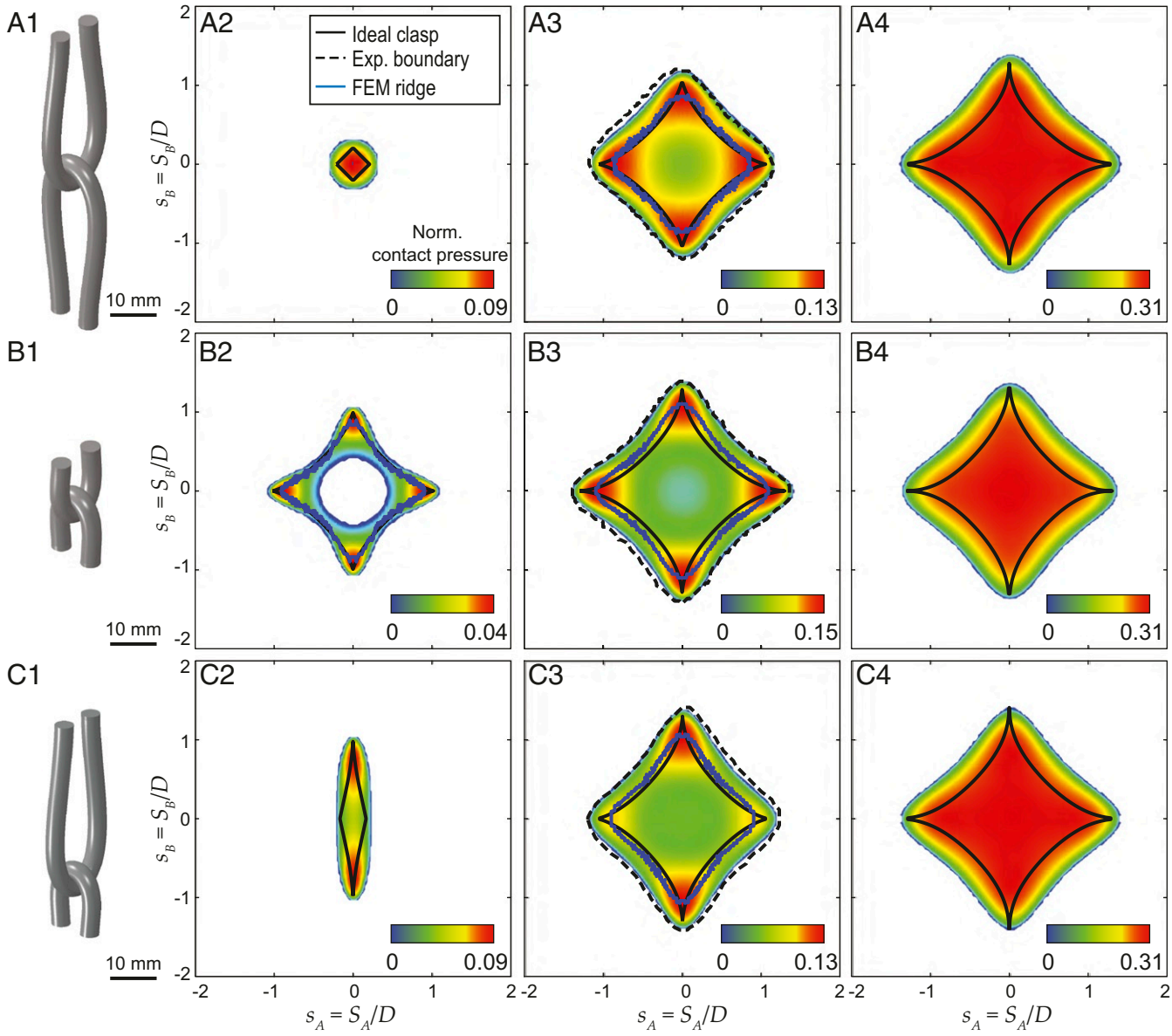

Fig. 3. Contact-pressure maps for nine different elastic orthogonal clasp equilibria. FEM-computed contact-pressure fields of elastic orthogonal clasps subject to three different sets of geometrical boundary conditions at three different values of the applied load: $l_A = l_B = 20$ (*A1*), $l_A = l_B = 7.5$ (*B1*), and $l_A = 20$, $l_B = 7.5$ (*C1*) (with the three physical configurations illustrated corresponding to the applied load $f_z = 0.005$). The pressure-field data for different values of normalized load $f_z = \{0.005, 0.05, 0.15\}$ are presented in (*A2*, *B2*, *C2*), (*A3*, *B3*, *C3*), and (*A4*, *B4*, *C4*), respectively. Blue solid lines, ridges extracted from the FEM-computed pressure field; dashed lines, experimentally (Exp.) observed boundaries of the contact surfaces; black solid lines, prediction of contact curves from ideal orthogonal clasp theory.

with its predicted gap between the tube surfaces close to the two centerline tips. A clarification of precisely which loading regimes give rise to a gap between the tip regions of the elastic orthogonal clasp would require further study.

The hybrid long/short rod configuration in Fig. 3*C2* exhibits a twofold symmetric pressure corresponding to the asymmetry between rod A and rod B. There are two pressure peaks along rod B, separated by a saddle with low pressure between the apices. Even in this extreme case, the ideal clasp diamond contact line yields a reasonable prediction of the extent of the actual contact surface in the elastic orthogonal clasp.

The Elastic Clasp with Sliding Friction

Leveraging the physical understanding gained above for the elastic orthogonal clasp with negligible friction, we next impose a relative motion between two elastically deformable rods in a clasp configuration, with finite friction, to extend the problem to obtain the *frictional sliding clasp*. There is a direct analogy between this system and the *capstan problem*, in which one deformable filament is wrapped in a planar configuration around a rigid drum, or capstan. The classic Euler–Eytelwein version of this problem (21, 31, 32) assumes that the capstan is a rigid cylinder and that the filament is perfectly flexible, with a negligible radius of curvature compared to the radius of the capstan. Then, the maximal possible ratio of high tension T_1 at one end to low tension T_0 at the other end is predicted by the well-known capstan relation,

$$\frac{T_1}{T_0} = e^{\mu\varphi}, \qquad [1]$$

where φ is the winding angle around the capstan, and μ is the friction coefficient (either static or dynamic depending on context) between the filament and the drum.

Our frictional sliding clasp load-displacement experiment can be viewed as a generalized capstan problem, in which the static, rigid drum is replaced by a second deformable rod, thereby adding elastic deformation in a nontrivial way. Motivated by this analogy, we seek to measure the change in the tension between the two ends of a rod sliding in steady state while wrapped around a second static, but deformable, rod. In our experiments (Fig. 4*A* and Movie S5), rod A is guided by two frictionless pulleys to thread around the clamped rod B. The rods are surface-treated to ensure robust Amontons–Coulomb frictional behavior with $\mu = 0.32 \pm 0.03$ (see details in *SI Appendix*, section 1.F). We measured the vertical force T necessary to displace the upper extremity of rod A at a constant velocity subject to a dead load $T_0 = Mg$, applied at the other extremity (where M is the mass of dead weight and g is the gravitational acceleration). Upon pulling with a prescribed velocity, the measured tension T first increases and then reaches a plateau value T_1 (Fig. 4*C* and *Materials and Methods*). We then quantified the steady tension ratio $K = T_1/T_0$ between the high- and low-tension strands, as a function of the nondimensional lower tension $t_0 = T_0/EA$, for different geometric configurations. Specifically, we adopt the same four sets of geometric parameters imposed in the global boundary conditions as for the static elastic orthogonal clasp experiments, namely, configurations 1 to 4 described in Fig. 2 *A–D*), but with the presence of the pulleys instead of clamps for rod A (Fig. 4 *B1–B4*). In *SI Appendix*, section 4.B, we show that our long sliding rod (rod A) mainly carries an internal tensile force (i.e., parallel to the tangent of the rod centerline) far from the contact region with rod B.

In Fig. 4*D*, we plot the experimental tension ratio K (data points) as a function of the dimensionless lower tension t_0 imposed by the dead load. We observe that all $K(t_0)$ increase monotonically with t_0, albeit with significant differences for the various imposed geometrical configurations in either rod A or rod B. In parallel to the experiments, we carried out FEM numerical simulations of the steady-state frictional sliding elastic clasp (solid lines; see *Materials and Methods*, *SI Appendix*, section 3, and Movie S6 for details of the simulations), finding good agreement with the experimental data (mean difference of $\approx 4.2\%$). The experimental and numerical data highlight the importance of the global opening angle imposed on the sliding rod; i.e., the angle between the tangents to rod A in the nearly straight tail regions far from contact, which are set experimentally by the distance between the pulleys. Indeed, we observed that $K(t_0)$ is lower when the pulleys are far apart (configuration 4, orange triangles) than when they are close to each other (configuration 1, green circles). The overall ordering of this difference in tension ratio for varying global opening angle in rod A is correctly predicted in the capstan Eq. **1** when applied with the wrapping angle φ interpreted as the global opening angle of rod A (dashed lines). (Note that the local opening angles, i.e., the angles between centerline tangents at touch-down and lift-off points, cannot be accessed experimentally because μCT data are not available for this experimental setup.) However, the simple capstan equation interpreted in this way is inadequate to explain

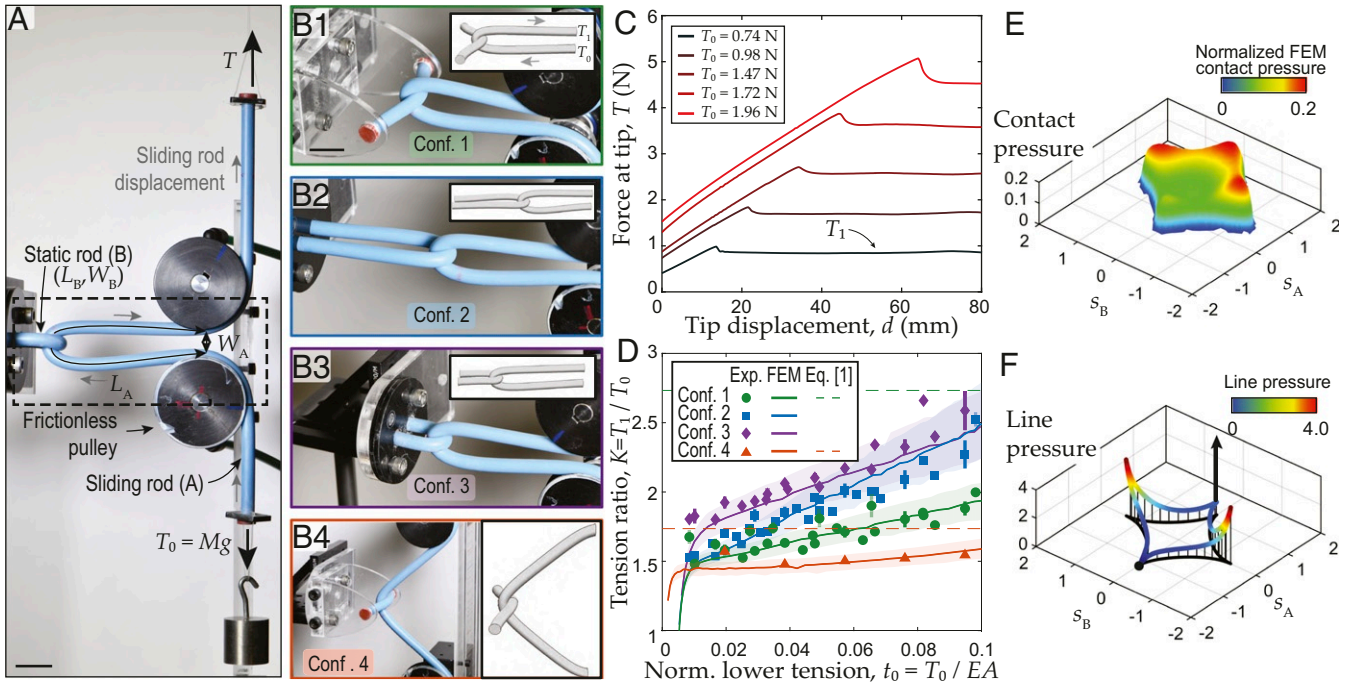

Fig. 4. Friction-induced tension gain in the sliding elastic clasp. (*A*) Experimental apparatus used to measure the tension ratio in different geometric configurations (Conf.). (Scale bar: 20 mm.) (*B1–B4*) Adaptation of configurations 1, 2, 3, and 4 described in Fig. 2 to allow for the sliding of rod A around the static rod B. (*C*) Experimentally measured upward force T in the upper segment of the sliding rod A as a function of the upward displacement d of the upper tip. (*D*) Ratio $K = T_1/T_0$ between the steady-state value of T (plateau in *C*) and the value of the dead load T_0 applied to the lower end of rod A, plotted as a function of the normalized dead load $t_0 = T_0/EA$ for the four different configurations. Experimental and FEM data are presented. The shaded regions correspond to the sensitivity of the FEM computation to the experimental uncertainty of the measured friction coefficient ($\mu = 0.32 \pm 0.03$). The horizontal dashed lines are the predictions from the capstan relation Eq. **1** applied to the global opening angle. (*E*) Representative contact-pressure map in the contact region obtained from the FEM simulation of configuration 3, at a normalized dead load of $t_0 = 0.05$ (the pressure is normalized by EA/D^2). (*F*) Linear pressure map of the ideal clasp, where it can be computed analytically that for a maximum tension growth equilibrium, the linear pressure vanishes at the touch-down point (black circle), but has a singular Delta function at the lift-off corner (represented by a black arrow).The qualitative features of the linear pressure field (force per unit length) shown in *F* match those of the pressure field (force per unit area) evaluated along its ridge lines, as shown in *E*.

our data because it predicts that the tension ratio should be independent of both t_0 and the imposed geometry on the static rod B; neither of these predictions is close to being accurate. Specifically, our results reveal the essential role of the static rod B; the tension-ratio response is significantly larger when the static rod wraps further around the sliding rod. For example, the tension ratio of configuration 3 (where the static rod is initially short with ends close to each other) is larger than the tension ratio for configuration 1, by 21% at $t_0 = 0.05$.

The limitations of the simple capstan relation in predicting the experimental data are consistent with the observation made above that a single elastic rod wrapped around a rigid cylindrical capstan, with its simple, single contact line, is inadequate to accurately describe local opening angles of an elastic clasp configuration. It is the local opening angles that are strongly related to the detailed contact geometry, which sets the maximal tension ratio $K(t_0)$. The mismatch between the capstan equation and our results stems from the nontrivial dependence of the local opening angles of the sliding and static rods on the applied tension t_0 and the associated changes in the contact set.

The detail of the contact-region interactions, including sliding friction, can be further probed via FEM. In Fig. 4*E*, we plot the pressure field between the two rods for the frictional sliding clasp configuration of Fig. 4*B3* (configuration 3). Just as in the static, frictionless case, the support of the contact-pressure map in the presence of friction displays the familiar diamond shape, and, again, there are strong heterogeneities. Now, however, we observe only three pressure peaks in the (s_A, s_B)-plane: two at the extreme values of s_B and one at the high-tension, or lift-off, end along s_A, where the pressure is largest. The symmetry along rod A is now broken, and the pressure at the touch-down end of the contact set is extremely low. As a first step toward understanding these qualitative features in the contact-pressure distribution for the sliding elastic clasp, in *SI Appendix*, section 4.F, we present a hybrid analysis of the ideal orthogonal clasp. In this framework, the shape of tube B is frozen to form a rigid tubular capstan with its own intricate geometry and local opening angle, around which the flexible tube A can reptate, with the contact set remaining identical with the static case (i.e., a closed, curvilinear, diamond-shaped line). In this idealized context, and as a consequence of moment balance on the positive radius flexible tube A, it can be derived (*SI Appendix*, section 4.E) that, in the presence of friction, the linear pressure distribution giving rise to the maximal possible tension ratio vanishes at the touch-down point, and has a Dirac delta function singularity at the lift-off point, as illustrated in Fig. 4*F*. Despite the strong simplifying assumptions in this ideal geometric capstan model, the numerical predictions for its linear pressure density have a striking qualitative similarity to the surface-pressure distributions for the elastic orthogonal clasp as computed in FEM simulations in Fig. 4*E*.

Conclusions

Despite the apparent simplicity of having only two elastic filaments in contact, our experiments and FEM computations on the orthogonal clasp system have revealed highly nontrivial behaviors. Throughout, we have obtained a good quantitative fit between experiment and FEM simulation of the elastic orthogonal clasp, in both static and sliding versions. For our first set of static experiments (with negligible frictional effects), this quantitative comparison was between 3D volumetric data on equilibrium configurations, including the surface patches that make up the contact set. For the second set of experiments, addressing sliding friction, the quantitative comparison was between load-displacement responses.

With the good match between experiment and FEM simulation established, we then further considered contact-pressure data that were not directly observable in experiment, but were available from FEM numerics. The contact-pressure fields are, of course, localized within the surface contact sets. However, in both static and sliding contexts, we specifically found that the contact-pressure field between the two filaments is strongly heterogeneous. This pressure field has high values concentrated on a curvilinear diamond pattern of four ridges linking isolated peaks in the pressure field; there are four peaks and twofold reflexional symmetry in the static case, but only three peaks and onefold symmetry in the sliding case. In both static and sliding cases, the ridge lines and peaks always arise rather close to the boundaries of the contact set, and the pressures in the interior of the contact region are comparatively low, corresponding to a central valley, surrounded by the ridges.

We qualitatively explained these striking ridge features observed in the FEM pressure fields in terms of the curvilinear diamond pattern of contact lines that arise in a version of the geometric, 1D theory of the ideal orthogonal clasp, which assumes no bending stiffness and which precludes any stretch in the tube centerline or deformation of cross-sections. The accuracy with which the contact lines in the idealized model predict the location of the pressure ridges in the fully elastic case for a wide range of loadings is all the more remarkable, given the scale of the deformation of cross-sections observed in both experiment and FEM for the elastic case. Specifically, in the static problem, the four peaks in pressure arise very close to the four apices of the curvilinear diamond pattern of the ideal contact lines. For the sliding problem, a version of a V-belt, double contact line, capstan problem constructed from the frictionless ideal orthogonal clasp problem qualitatively explains the asymmetric roles of touch-down and lift-off points in the pressure distribution, as manifested in there being only three peaks of pressure in the sliding case.

We hope that our findings will instigate future theoretical model developments that consider the intricate coupling of elasticity and contact geometry of filaments with a small, but nonvanishing, diameter. Future 1D models that might reach beyond our current qualitative explanations of experimental data and intensive FEM simulations, to quantitative predictions of tube equilibria with tight contact, should combine the detailed geometry captured by the idealized, flexible tube description with the incorporation of elasticity, both through a bending stiffness for the centerline and in allowing cross-sectional deformation. Standard Kirchhoff and Cosserat rod models can already capture such elastic effects, but existing applications of rod theories involving contact assume highly simplified contact sets, which we have shown to be insufficient to yield accurate predictions in the context of tight coiling of tubes with small, but nonvanishing, radius. However, the construction of a numerically tractable, 1D theory that combines both elasticity and detailed contact geometry is not in and of itself entirely straightforward. Such efforts would significantly impact the homogenization schemes necessary to predictively describe more intricate networks of filaments, such as knits, knots, and weaves, starting from the elastic clasp as a building block.

Materials and Methods

Fabrication of the Rods for μCT Imaging. For the *static elastic orthogonal clasp* experiment, elastomeric rods were fabricated through casting by using silicone-based polymers, with a coaxial geometry comprising 1) a bulk core, 2) a thin physical centerline fiber, and 3) an outer coating layer. The bulk core was fabricated out of Vinyl PolySiloxane (VPS-16, Elite Double 16 Fast, Zhermack), whereas the physical centerline fiber and the outer coating were made out of the Solaris polymer (Smooth-On). The overall diameter of the resulting rod was $D = 8.5$ mm. Additional fabrication details are provided in *SI Appendix*, section 1.A.

μCT. Tomographic imaging of the elastic clasp configurations was performed by using a μCT 100 (Scanco) machine for the static elastic orthogonal

clasps in configurations 1 and 3 and an Ultra-Tom (RX-Solutions) machine for configurations 2 and 4. An in-house postprocessing algorithm (written in MATLAB 2019b, MathWorks) was used to extract the coordinates of the centerline of the rods, as well as those of the rod–rod contact surface, from the volumetric μCT images (*SI Appendix*, section 1.B).

Fabrication of the Rods for Mechanical Testing. For mechanical testing, the rods were fabricated out of Vinyl PolySiloxane of two different grades: VPS-16 (Elite double 16 Fast, Zhermack) and VPS-32 (Elite double 32, Zhermack). The rods were cast in straight acrylic tubes of inner diameter $D = 8$ mm. Further details are provided in *SI Appendix*, section 1.E.

Mechanical Testing. For the *sliding orthogonal clasp* experiment, we quantified the high-to-low tension ratio in the two ends of a rod sliding around another by performing force-displacement experiments on a mechanical testing machine (Instron 5943 with a 50-N load-cell). These tests used frictionless rotating pulleys to guide the sliding rod. The upper end of the sliding rod was pulled upward at constant velocity $U = 3$ mm/s, while measuring the pulling force T. See further details in *SI Appendix*, section 1.F.

Finite Element Modeling. FEM simulations were performed by using the software package ABAQUS/STANDARD to numerically compute the equilibria of the elastic static and sliding orthogonal clasps. The elastic rods were meshed with 3D brick elements with reduced integration and hybrid formulation (C3D8RH), with a Neo-Hookean hyperelastic material model. The geometry, meshing, and loading sequences are detailed in *SI Appendix*, section 3.

Data Availability. Some study data are available upon request.

ACKNOWLEDGMENTS. We thank B. Audoly and S. Neukirch for fruitful discussions, as well as G. Perrenoult and P. Turberg for advice on μCT tomography. P.J. was supported by Fonds National de la Recherche, Luxembourg Grant 12439430. H.S., A.F., and J.H.M. were partially supported by Swiss National Science Foundation Grant 200020-18218 (to J.H.M.), and T.G.S. was supported by Grants-in-Aid for Japan Society for the Promotion of Science Overseas Research Fellowship 2019-60059.

1. B. L. Hardy *et al.*, Direct evidence of Neanderthal fibre technology and its cognitive and behavioral implications. *Sci. Rep.* **10**, 4889 (2020).
2. T. L. Buckner, R. A. Bilodeau, S. Y. Kim, R. Kramer-Bottiglio, Roboticizing fabric by integrating functional fibers. *Proc. Natl. Acad. Sci. U.S.A.* **117**, 25360–25369 (2020).
3. L. Euler, *Methodus Inveniendi Lineas Curvas Maximi Minimive Proprietate Gaudentes Sive Solutio Problematis Isoperimetrici Latissimo Sensu Accepti* (Opera Mathematica, Springer Science and Business Media, Berlin, Germany, 1952), vol. 1.
4. L. M. Landau, E. M. Lifshitz, *Theory of Elasticity* (Course of Theoretical Physics, Butterworth-Heinemann, Oxford, UK, 1986), vol. 7.
5. G. Kirchhoff, Ueber das gleichgewicht und die bewegung eines unendlich dünnen elastischen stabes. *J. für die Reine Angewandte Math.* **56**, 285–313 (1859).
6. G. Kirchhoff, *Mechanik (Vorlesungen über Mathematische Physik*, BG Teubner, Leipzig, Germany, 1876), vol. 1.
7. T. G. Sano, T. Yamaguchi, H. Wada, Slip morphology of elastic strips on frictional rigid substrates. *Phys. Rev. Lett.* **118**, 178001 (2017).
8. A. Goriely, S. Neukirch, Mechanics of climbing and attachment in twining plants. *Phys. Rev. Lett.* **97**, 184302 (2006).
9. S. Poincloux, M. Adda-Bedia, F. Lechenault, Geometry and elasticity of a knitted fabric. *Phys. Rev. X.* **8**, 021075 (2018).
10. P. Ayres, A. G. Martin, M. Zwierzycki. "Beyond the basket case: A principled approach to the modelling of kagome weave patterns for the fabrication of interlaced lattice structures using straight strips" in Proceedings: Advances in Architectural Geometry 2018, L. Hesselgren et al., eds. (Klein Publishing Gmbh, Wien, Austria, 2018), pp. 72–93.
11. J. Vekhter, J. Zhuo, L. F. Gil Fandino, Q. Huang, E. Vouga, Weaving geodesic foliations. *ACM Trans. Graph.* **38**, 1–22 (2019).
12. C. Baek, A. O. Sageman-Furnas, M. K. Jawed, P. M. Reis, Form finding in elastic gridshells. *Proc. Natl. Acad. Sci. U.S.A.* **115**, 75–80 (2018).
13. C. Baek, P. M. Reis, Rigidity of hemispherical elastic gridshells under point load indentation. *J. Mech. Phys. Solid.* **124**, 411–426 (2019).
14. T. Yamaguchi, Y. Onoue, Y. Sawae, Topology and toughening of sparse elastic networks. *Phys. Rev. Lett.* **124**, 068002 (2020).
15. N. Stoop, F. K. Wittel, H. J. Herrmann, Morphological phases of crumpled wire. *Phys. Rev. Lett.* **101**, 094101 (2008).
16. G. M. Grason, Braided bundles and compact coils: The structure and thermodynamics of hexagonally packed chiral filament assemblies. *Phys. Rev. E.* **79**, 041919 (2009).
17. A. Ward *et al.*, Solid friction between soft filaments. *Nat. Mater.* **14**, 583–588 (2015).
18. A. Panaitescu, G. M. Grason, A. Kudrolli, Measuring geometric frustration in twisted inextensible filament bundles. *Phys. Rev. E* **95**, 052503 (2017).
19. A. Panaitescu, G. M. Grason, A. Kudrolli, Persistence of perfect packing in twisted bundles of elastic filaments. *Phys. Rev. Lett.* **120**, 248002 (2018).
20. P. B. Warren, R. C. Ball, R. E. Goldstein, Why clothes don't fall apart: Tension transmission in staple yarns. *Phys. Rev. Lett.* **120**, 158001 (2018).
21. J. H. Maddocks, J. B. Keller, Ropes in equilibrium. *SIAM J. Appl. Math.* **47**, 1185–1200 (1987).
22. B. Audoly, N. Clauvelin, S. Neukirch, Elastic knots. *Phys. Rev. Lett.* **99**, (2007).
23. M. K. Jawed, P. Dieleman, B. Audoly, P. M. Reis, Untangling the mechanics and topology in the frictional response of long overhand elastic knots. *Phys. Rev. Lett.* **115**, (2015).
24. V. P. Patil, J. D. Sandt, M. Kolle, J. Dunkel, Topological mechanics of knots and tangles. *Science* **367**, 71–75 (2020).
25. C. Baek, P. Johanns, T. G. Sano, P. Grandgeorge, P. M. Reis, Finite element modeling of tight elastic knots. *J. Appl. Mech.* **88**, 2020.
26. P. Johanns *et al.*, The shapes of physical trefoil knots. *Extreme Mech. Lett.* **43**, 101172 (2021).
27. O. Gonzalez, J. H. Maddocks, Global curvature, thickness, and the ideal shapes of knots. *Proc. Natl. Acad. Sci. U.S.A.* **96**, 4769–4773 (1999).
28. M. Carlen, B. Laurie, J. Maddocks, J. Smutny, "Biarcs, global radius of curvature, and the computation of ideal knot shapes" in *Physical and Numerical Models in Knot Theory and Their Application to the Life Sciences*, J. A. Calvo, K. C. Millett, E. J. Rawdon, A. Stasiak, eds. (Series on Knots and Everything, World Scientific Publishing Co. Pte. Ltd., Singapore, 2005), vol. 36, pp. 75–108.
29. E. L. Starostin, A constructive approach to modelling the tight shapes of some linked structures. *Forma* **18**, 263–293 (2003).
30. S. S. Antman, *Nonlinear Problems of Elasticity* (Springer, New York, NY, 2005).
31. L. Euler, Remarques sur l'effet du frottement dans l'equilibre. *Memoires de l'academie des sciences de Berlin* **18**, 265–278 (1769).
32. J. A. Eytelwein, *Handbuch der Statik fester Körper: Mit Vorzüglicher Rücksicht auf ihre Anwendung in der Architektur* (Reimer, Berlin, Germany, 1832), vol. 1.